# On Material Modeling by Polygonal Discrete Elements

B. Schneider, G.A. D'Addetta and E. Ramm

**Abstract** The contribution gives an overview on a discrete element model with polygonal particles in a two-dimensional setting allowing the simulation of granular as well as quasi-brittle material response. It briefly describes the basic formulation for geometry and applied contact models in normal and tangential direction, supplemented by friction on a background plate. Special emphasis is put on modeling of cohesion; three different models with an increasing complexity are introduced, namely an overlay brittle beam lattice, a beam with damage and an interface model. Homogenization of the discrete particle response is utilized deriving variables like stresses and strains for an interpretation in the context of classical and micropolar continua. Several numerical examples for different loading scenarios are added, among them the simulation of a quasi-brittle material sample with a heterogeneous microstructure. In addition conceptual small scale experiments with regular particles of steel nuts have been performed; results from tests and simulations for samples with and without cohesion are compared.

## 1 Introduction

The notion of "particle method" is not unique and might even cause confusion, for example when it is used for special discretization concepts of continuum mechanics problems like the Smoothed Particle Hydrodynamic Method (SPH) or the Particle Finite Element Method (PFEM). In the present contribution it is used in the classical sense of the Discrete Element Method (DEM), an area becoming a very successful discipline of its own with applications in many different fields, see the reviews [2–5, 20].

B. Schneider · G.A. D'Addetta · E. Ramm
Institute of Structural Mechanics, Stuttgart University, Pfaffenwaldring 7, 70550 Stuttgart, Germany; e-mail: {schneider, gad, ramm}@ibb.uni-stuttgart.de

E. Oñate and R. Owen (eds.), *Particle-Based Methods*, Computational Methods in Applied Sciences 25, DOI 10.1007/978-94-007-0735-1_6,

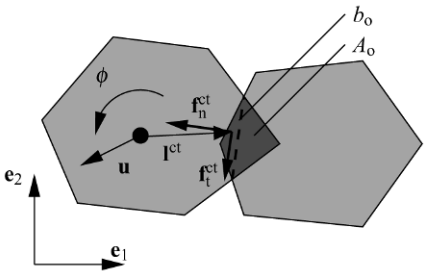


**Fig. 1** Geometry of contact

The present discrete element model describes the mechanical response of materials consisting of separable solid particles on a mesoscopic scale. These materials maybe granular like sand, soil or powder. However the particles can also be initially glued together like in concrete or ceramics and may disintegrate during loading. These materials are sometimes denoted as cohesive-frictional or quasi-brittle. In case the cohesion either initially does not exist or disappears during loading the particles interact only by contact.

The geometry of particles can be modeled by smooth contours like circles (2D)/spheres (3D), ellipses/ellipsoids and superellipses/superellipsoids or with sharp corners as polygons/polyhedrons, with triangles/tetrahedrons being a special case. They also may be composed of several elementary geometrical solids. It is obvious that the complexity of the geometrical description varies depending on the number of parameters involved; it comes without saying that the simplest model applying circles/spheres with the radius as the only parameter is by far the most often version in particle simulations.

## 2 Basic Discrete Element Method

In the present study we concentrate on the two-dimensional case applying polygonal particles; although the 2D-model is a coarse simplification of a real material sample it allows to study the mechanical complexity of polygons since particles often exhibit shapes with sharp corners. The applied DEM model with convex polygonal particles is based on the original work of Tillemans and Herrmann [21]. It utilizes a special form of Voronoi tessellation denoted as vectorizable random lattice for mesh generation developed in [19].

The modified version applied in this study has already been described in detail in [7–10], so that the model is only briefly outlined in the sequel. The particles are assumed to be rigid and unbreakable and can interact by contact as well as cohesive forces. The three degrees of freedom of each particle – two translations of the center of mass and one rotation around it – are summarized in the generalized displacement $\mathbf{u}^g = [\mathbf{u}^T, \phi]^T = [u_1, u_2, \phi_3]^T$, see Figure 1. The balance of linear and angular momentum of each individual particle yield the equations of motion

$$\mathbf{M}^{\mathrm{g}}\ddot{\mathbf{x}}^{\mathrm{g}} = \mathbf{f}^{\mathrm{g}} + \hat{\mathbf{f}}^{\mathrm{g}}\,. \tag{1}$$

$\mathbf{M}^{\mathrm{g}}$ and $\ddot{\mathbf{x}}^{\mathrm{g}}$ are the generalized diagonal mass matrix and particle acceleration

$$\mathbf{M}^{\mathrm{g}} = \begin{bmatrix} M & 0 & 0 \\ 0 & M & 0 \\ 0 & 0 & \Theta \end{bmatrix}; \qquad \ddot{\mathbf{x}}^{\mathrm{g}} = \begin{bmatrix} \ddot{x}_1 \\ \ddot{x}_2 \\ \ddot{\varphi} \end{bmatrix}. \tag{2}$$

$M$ and $\Theta$ express the particle mass and mass moment of inertia, respectively. $\ddot{x}_1$ and $\ddot{x}_2$ are the accelerations in $\mathbf{e}_1$- and $\mathbf{e}_2$-direction and $\ddot{\varphi}$ is the angular acceleration. The right hand side comprises the forces and torques from particle interaction $\mathbf{f}^{\mathrm{g}} = [\mathbf{f}^{\mathrm{T}}, m]^{\mathrm{T}}$ and from external loads $\hat{\mathbf{f}}^{\mathrm{g}} = [\hat{\mathbf{f}}^{\mathrm{T}}, \hat{m}]^{\mathrm{T}}$, for example gravity. $\mathbf{f}^{\mathrm{g}}$ is composed of a contribution from contact $\mathbf{f}^{\mathrm{g,ct}}$ with $n_{\mathrm{ct}}$ contacting particles and a contribution from cohesion $\mathbf{f}^{\mathrm{g,ch}}$ with $n_{\mathrm{ch}}$ bonded particles

$$\mathbf{f}^{\mathrm{g}} = \mathbf{f}^{\mathrm{g,ct}} + \mathbf{f}^{\mathrm{g,ch}} = \sum_{j=1}^{n_{\mathrm{ct}}} \mathbf{f}_j^{\mathrm{g,ct}} + \sum_{j=1}^{n_{\mathrm{ch}}} \mathbf{f}_j^{\mathrm{g,ch}}\,. \tag{3}$$

Contact and cohesive forces are introduced in the subsequent sections.

For all particles of a sample the equations of motion (1) result in a coupled system of ordinary differential equations; they are numerically integrated by a predictor-corrector scheme introduced in [14] and used also in [1]. We use an explicit version with a predictor and one corrector step which takes into account time derivatives of the displacement up to fifth order; for details of the implemented version of the time integration, see [7].

## 3 Models for Contact

The contact search is in general the most time consuming part in particle dynamics and needs special attention from efficiency point of view, for reviews on various algorithms confer [1, 25]. In general these schemes can be classified into body- and spatial-based categories. In the present study a multilevel approach on the basis of a spatial-based linked cell algorithm is adopted for the preparation of neighborhood lists, compare [1]. This process is described in detail in [7, 21].

When two particles contact each other a small overlap $A_{\mathrm{o}}$ of the rigid bodies is allowed resulting in repulsing contact forces as indicated in Figure 1. The contact force is split into a normal and a tangential component in $\mathbf{n}$- and $\mathbf{t}$-direction

$$\mathbf{f}^{\mathrm{ct}} = \mathbf{f}_{\mathrm{n}}^{\mathrm{ct}} + \mathbf{f}_{\mathrm{t}}^{\mathrm{ct}} = f_{\mathrm{n}}^{\mathrm{ct}}\mathbf{n} + f_{\mathrm{t}}^{\mathrm{ct}}\mathbf{t}\,. \tag{4}$$

They are applied at the midpoint of the contact line $b_{\mathrm{o}}$, denoted the contact point. Due to the lever $\mathbf{l}^{\mathrm{ct}}$ they also give rise to a torque $m^{\mathrm{ct}}$ around the center of mass.

### 3.1 Normal Direction

For the normal force two alternative models are investigated both consisting of an elastic and a viscous part.

The first one was introduced in [21] as

$$\mathbf{f}_{\mathrm{n}}^{\mathrm{ct}} = -\left(\frac{E_{\mathrm{n}}^{(1)} A_{\mathrm{o}}}{d_{\mathrm{c}}} + M_{\mathrm{eff}}\gamma_{\mathrm{n}} v_{\mathrm{n}}\right)\mathbf{n}\,. \tag{5}$$

$E_{\mathrm{n}}^{(1)}$ is the elastic "contact stiffness" which plays the role of a penalty parameter. $A_{\mathrm{o}}$ is the overlapping area, see Figure 1. $\gamma_{\mathrm{n}}$ denotes the viscous damping coefficient and $v_{\mathrm{n}}$ is the relative velocity in normal direction. $d_{\mathrm{c}}$ describes a characteristic length and $M_{\mathrm{eff}}$ is the effective mass of two contacting particles $i$ and $j$

$$\frac{1}{d_{\mathrm{c}}} = \frac{1}{d_{\mathrm{c},i}} + \frac{1}{d_{\mathrm{c},j}}\,; \qquad M_{\mathrm{eff}} = \frac{M_i M_j}{M_i + M_j}\,. \tag{6}$$

$d_{\mathrm{c},i}$ and $d_{\mathrm{c},j}$ are the diameters of equivalent circles having the same area as the two particles.

The second model combines an elastic force proposed in [13] with a viscous force

$$\mathbf{f}_{\mathrm{n}}^{\mathrm{ct}} = -\left(E_{\mathrm{n}}^{(2)} A_{\mathrm{o}} b_{\mathrm{o}} + M_{\mathrm{eff}}\gamma_{\mathrm{n}} v_{\mathrm{n}}\right)\mathbf{n}\,. \tag{7}$$

The elastic part can be derived from a potential and is therefore energy conserving. $b_{\mathrm{o}}$ is length of the contact line as indicated in Figure 1.

### 3.2 Tangential Direction

Again two different models have been used for the tangential force. The first one [21] selects the minimum of a frictional and a viscous force

$$\mathbf{f}_{\mathrm{t}}^{\mathrm{ct}} = -\mathrm{sgn}(v_{\mathrm{t}})\min\left(\mu_{\mathrm{t}}\|\mathbf{f}_{\mathrm{n}}^{\mathrm{ct}}\|,\, M_{\mathrm{eff}}\gamma_{\mathrm{t}}|v_{\mathrm{t}}|\right)\mathbf{t}\,. \tag{8}$$

$\mu_{\mathrm{t}}$ is the friction coefficient and $\gamma_{\mathrm{t}}$ the viscous parameter. $v_{\mathrm{t}}$ denotes the relative velocity in tangential direction.

For the second version an elasto-plastic model with Coulomb frictional yield limit similar to the one in [6] has been chosen

$$\mathbf{f}_{\mathrm{t}}^{\mathrm{ct}} = -E_{\mathrm{t}} u_{\mathrm{t}}^{\mathrm{el}}\mathbf{t}\,; \qquad \mathcal{F} = \|\mathbf{f}_{\mathrm{t}}^{\mathrm{ct}}\| - \mu_{\mathrm{t}}\|\mathbf{f}_{\mathrm{n}}^{\mathrm{ct}}\| \le 0\,. \tag{9}$$

$u_{\mathrm{t}}^{\mathrm{el}}$ describes the relative elastic displacement component in tangential direction. $\mathcal{F}$ is the yield function again governed by the frictional parameter $\mu_{\mathrm{t}}$. This model is able to reproduce sticking as well as sliding friction.

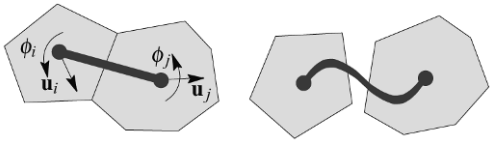


**Fig. 2** Overlay of beam lattice and beam deformations by particle movements

### *3.3 Contact with Background Plate*

In view of model tests described in Section 6 we also discuss the movement of a particle ensemble on a background plate. For this the force between each particle and the background medium has to be modeled in addition to the interaction between particles. Analogous to the tangential contact model (9) an elasto-plastic model with Coulomb friction is applied at each point on the particle surface contacting the background plate

$$\boldsymbol{\tau}_{\mathrm{b}}^{\mathrm{ct}} = -E_{\mathrm{b}}\mathbf{u}_{\mathrm{b}}^{\mathrm{el}}\,; \qquad \mathcal{F} = \|\boldsymbol{\tau}_{\mathrm{b}}^{\mathrm{ct}}\| - \mu_{\mathrm{b}}|\sigma_{\mathrm{b}}^{\mathrm{ct}}| \le 0\,. \tag{10}$$

$\sigma_{\mathrm{b}}^{\mathrm{ct}}$ is the normal stress between the particle surface and the background plate, for example resulting through gravity loads of the particles. The distributed shear stresses $\boldsymbol{\tau}_{\mathrm{b}}^{\mathrm{ct}}$ are integrated numerically to a resulting force and torque acting at the center of the particle.

## 4 Models for Cohesion

In the next step, in addition to the contact forces, cohesive or adhesive forces are introduced if the particles initially stick together or are bonded in their initial state. Cohesion is a complex phenomenon on a fine scale; in the present study we concentrate on models on a coarse scale as a compromise between sufficient realism and efficiency. We will discuss three different models with increasing complexity and expense.

### *4.1 Brittle Beam*

In this most simplistic representation cohesion is modeled on the structural level. A beam lattice consisting of small strain shear beams (Timoshenko beams) as an overlay model [16–18, 21] is introduced connecting the centers of mass of all neighbored particles as sketched in Figure 2. The beams are rigidly connected to the particles on both ends and do not possess any mass. Their stiffness can be derived from the elastic potential for beams representing cohesive forces

$$\Phi^{\mathrm{ch}} = \int_0^L \frac{1}{2} \begin{bmatrix} \varepsilon_{\mathrm{ax}} \\ \kappa \\ \gamma \end{bmatrix}^{\mathrm{T}} \underbrace{\begin{bmatrix} EA^{\mathrm{ch}} & 0 & 0 \\ 0 & EI^{\mathrm{ch}} & 0 \\ 0 & 0 & GA_{\mathrm{Q}}^{\mathrm{ch}} \end{bmatrix}}_{\mathbf{C}^{\mathrm{el}}} \begin{bmatrix} \varepsilon_{\mathrm{ax}} \\ \kappa \\ \gamma \end{bmatrix} \mathrm{d}L \,, \tag{11}$$

where $\varepsilon_{\mathrm{ax}}$, $\kappa$, $\gamma$ are the axial strain, curvature and transverse shear strain, respectively. The elastic material matrix $\mathbf{C}^{\mathrm{el}}$ contains the axial stiffness $EA^{\mathrm{ch}}$, bending stiffness $EI^{\mathrm{ch}}$ and shear stiffness $GA_{\mathrm{Q}}^{\mathrm{ch}}$ with Young's modulus $E$, cross sectional area $A$, moment of inertia $I$ and shear area $A_{\mathrm{Q}}$. From Eq. (11) the usual stiffness expression for a Timoshenko beam element can be derived

$$\begin{bmatrix} \mathbf{f}_i^{\mathrm{g,ch}} \\ \mathbf{f}_j^{\mathrm{g,ch}} \end{bmatrix} = \mathbf{K}_{ij}^{\mathrm{ch}} \begin{bmatrix} \mathbf{u}_i^{\mathrm{g}} \\ \mathbf{u}_j^{\mathrm{g}} \end{bmatrix} . \tag{12}$$

It yields the generalized forces $\mathbf{f}^{\mathrm{g,ch}}$ derived from the generalized displacements $\mathbf{u}^{\mathrm{g}}$ of the particles. Each beam deforms with the six degrees of freedom of the particles as shown in Figure 2 (right) leading to additional forces and torques on both particles $i$ and $j$ caused by vectors containing the generalized beam end forces.

The individual beam behaves initially elastic until a cracking criterion is satisfied

$$\left( \frac{\varepsilon_{\mathrm{ax}}}{\varepsilon_{\max}} \right)^2 + \frac{\max(|\phi_i|, |\phi_j|)}{\phi_{\max}} = 1 \,. \tag{13}$$

Cracking is allowed only if the axial strain $\varepsilon_{\mathrm{ax}}$ is positive and therefore only applied under tension. Concerning the bending, only the maximum value of the end rotations $\phi_i$ or $\phi_j$ is monitored. $\varepsilon_{\max}$ and $\phi_{\max}$ are given threshold values for breaking combined to the interaction or failure criterion (13). The beam connections representing cohesion are checked after each time step considering the updated coordinates of the centers of mass of the particles. Overstressed beams break and are removed from the calculation.

The present beam model represents an extremely brittle failure and sudden loss of cohesion in the sense of a "tension cut-off" criterion. It might however be extended by a softening type of gradual failure. It has to be kept in mind that the location for monitoring the cohesion is transferred from the contact zone to the centers of the particles. Despite of the mentioned limitations it can be stated that it is a very simple, inexpensive and easy to implement model. It is also well known that pure lattice models have been successfully applied for the simulation of quasi-brittle materials.

### *4.2 Beam with Damage*

In order to reproduce less brittle, i.e. more ductile failure behavior, a second still efficient model is introduced. It keeps the shear beam as structural model which de-

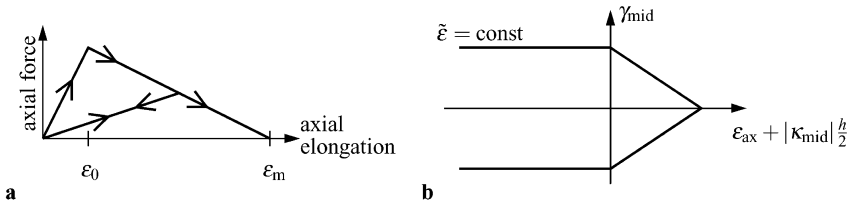


**Fig. 3** (a) Damage evolution and (b) damage surface

forms with the degrees of freedom of the particles; however in this case the failure of the beam is transferred to the cross section at the middle between two particles. The material model accounts for a successive degradation of the cohesive connection in the sense of a strain resultant criterion. For this purpose the elastic beam element with zero mass is enhanced by a damage model with softening instead of using the above introduced brittle failure criterion. The degradation of $E$ is represented by the usual factor $(1-d)$ where $d$ is the isotropic damage parameter yielding the elasto-damage material matrix

$$\mathbf{C}^{\text{ed}} = \begin{bmatrix} (1-Hd)EA^{\text{ch}} & 0 & 0 \\ 0 & (1-d)EI^{\text{ch}} & 0 \\ 0 & 0 & (1-d)GA_{\text{Q}}^{\text{ch}} \end{bmatrix}; \quad H = \begin{cases} 0 & \text{for } \varepsilon_{\text{ax}} \leq 0 \\ 1 & \text{for } \varepsilon_{\text{ax}} > 0 \end{cases}. \tag{14}$$

The Heaviside function $H$ is inserted in order to represent the unilateral character for the axial stiffness, only present in tension but not in compression.

The evolution of damage is defined by linear softening exemplarily depicted in Figure 3a for axial elongation

$$d = \begin{cases} 0 & : \varepsilon^* \leq \varepsilon_0 \\ \dfrac{\varepsilon_{\text{m}}}{\varepsilon^*} \dfrac{\varepsilon^* - \varepsilon_0}{\varepsilon_{\text{m}} - \varepsilon_0} & : \varepsilon_0 < \varepsilon^* < \varepsilon_{\text{m}} \\ 1 & : \varepsilon^* \geq \varepsilon_{\text{m}} \end{cases}; \qquad \varepsilon^*(t) = \max_{0 \leq \tau \leq t} \tilde{\varepsilon}(\tau)\,. \tag{15}$$

$\varepsilon^*$ is the largest strain level reached at each time. The maximum strain level is denoted by $\varepsilon_{\text{m}}$ when the beam section is completely damaged ($d = 1$) and fails. The damage mode is characterized by a combined axial strain-bending-shear failure at the middle between two particles, defined by the equivalent strain

$$\tilde{\varepsilon} = < \varepsilon_{\text{ax}} + |\kappa_{\text{mid}}| \frac{h}{2} > + |\gamma_{\text{mid}}|\,. \tag{16}$$

The damage surface is displayed in Figure 3b. The measure combines the strains from axial elongation $\varepsilon_{\text{ax}}$, curvature $\kappa_{\text{mid}}$ and shear deformation $\gamma_{\text{mid}}$ at the middle cross section; $h$ is the height of the beam. As indicated by the Macaulay bracket for the first part only tensional strains are considered. They are evaluated at the outermost fiber (marked by a cross in Figure 4) where the material is stretched most;

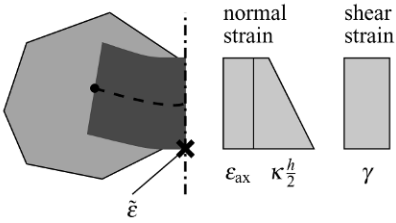


**Fig. 4** Strains of beam

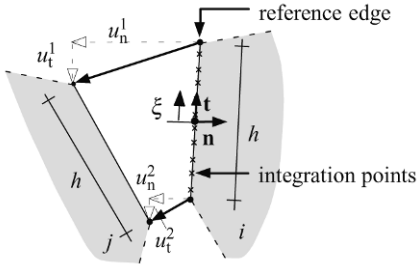


**Fig. 5** Numerical integration with reference edge

the strain distribution following beam theory is displayed in Figure 4. According to the assumed kinematics the shear strain $\gamma$ is constant across the height so that only its absolute value enters the equivalent strain; it is the only variable which defines the failure under compression.

This damage model exploiting the kinematics of a beam at the middle between two particles is able to reproduce a more ductile failure behavior for cohesion being still numerically inexpensive.

## *4.3 Softening Interface*

The third and most advanced model refines the previous version. A continuous connection between two particles in a sense of a zero-thickness interface element is assumed. The model adopts again the kinematics with a linear displacement field across the contact line as in the previous beam model ("*plane sections remain plane*") however allows a complex stress distribution after successive debonding of the interface. This material degradation at each point of the interface is described by small strain, non-associated plasticity coupled in normal and tangential direction by a two-surface Mohr–Coulomb yield function [24].

The evolving stress distribution is numerically integrated at a finite number of points along the interface height $h$, computing the resulting force and torque on the particle similar to stress resultants in a beam, see Figure 5. The particle $i$ has been chosen as master; its bond has been selected as reference edge. The local coordinate system **n**-**t** defining the components of the displacement field as well as the normalized coordinate $\xi$ for integration is fixed along this edge. Having this discretization

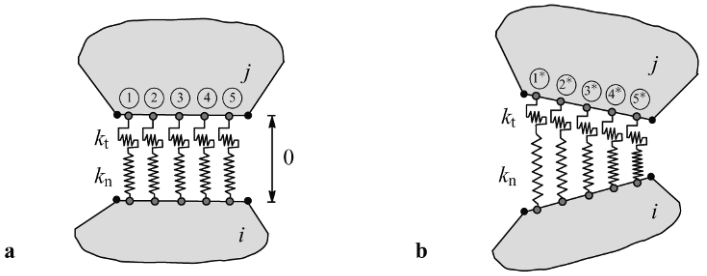


**Fig. 6** Idealization of interface by springs in (a) undeformed and (b) deformed stage

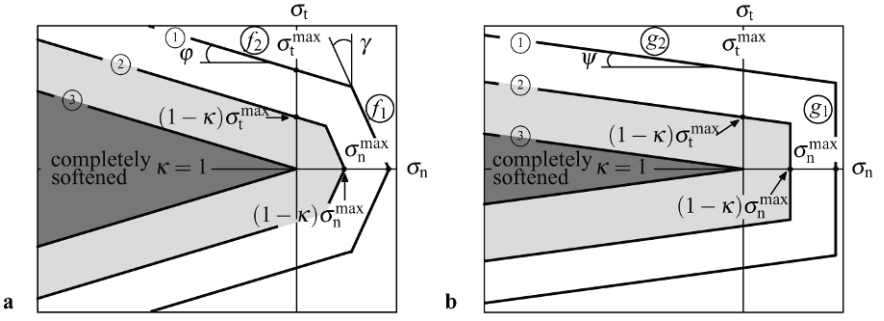


**Fig. 7** (a) Yield surface and (b) plastic potential for interface in biaxial stress plane

in mind one could idealize the model as a series of non-linear springs coupled in normal and tangential direction as depicted for an undeformed (with zero thickness) and deformed stage in Figure 6. In the elastic regime uncoupled stiffnesses $k_n$ and $k_t$ are assumed for the springs in both directions.

This interface model has been documented in detail in [7, 8, 11]; here only some basic ingredients are mentioned. Figure 7 displays the yield surface and the plastic potential in the biaxial $\sigma_t$-$\sigma_n$ plane, defined by the functions $f_1/f_2$ and $g_1/g_2$, respectively. Besides the limit values for the stresses $\sigma_{n/t}^{max}$ the angles $\gamma$ and $\varphi$ as well as $\psi \neq \varphi$ control the shape of failure envelopes. In these diagrams $\kappa$ denotes the softening variable; three stages are marked from the initial undamaged state ①, an intermediate partially damaged situation ② to the completely softened state ③. The distinction between yield function and plastic potential is necessary because certain geomaterials do not obey the normality condition.

The softening driven by the plastic displacements $u_n^p$ and $u_t^p$ at the integration points ("springs") is controlled by predefined fracture energies $G_{f,n}$ and $G_{f,t}$. Two different softening evolutions for tension and shear are introduced, see Figures 8a and b. The linear softening functions describe the uncoupled cases when either a pure tension or a pure shear failure mode governs the degradation of the interface. A simultaneous coupled tensile and shear softening is treated as linear combination of both modes as depicted in Figure 8c for the extreme case of $\kappa = 1$.

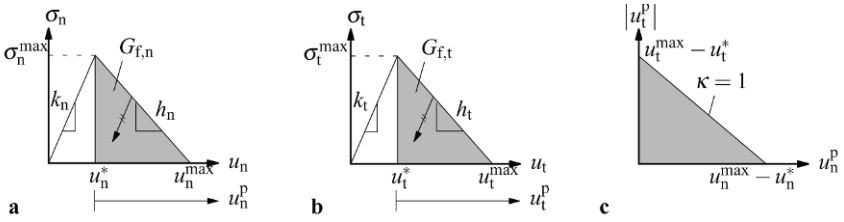


**Fig. 8** Evolution of softening for (a) tension, (b) shear and (c) a combination thereof

The explicit mathematical model for the interface material is described in [7, 8], where also the numerical realization is explained. It follows the usual small strain plasticity concept, applying return algorithms for the time integration with an elastic predictor and a plastic corrector.

When all integration points have reached complete softening the bond is detached. The standard contact as described in Section 3 comes into play once two initially bonded particles with broken bond again contact each other.

## 5 Homogenization

### *5.1 Motivation*

Homogenization is a common procedure in order to determine the response of heterogeneous materials on a macroscale. It is well known that these concepts are based on the existence of a clear scale separation, also known as Hashin's MMM (Micro-Meso-Macro) principle of homogenization [15]. In the present context it means that there is a distinct scale difference between the particles (microscale) and the entire structure (macroscale) allowing establishing a Representative Volume Element (RVE) on an intermediate mesoscale; this is expressed by the condition $D \gg d \gg \delta$ as indicated in Figure 9 for an arbitrary particle ensemble. In contrast to the usual application of RVEs determining constitutive relations and material parameters for a macroscopic analysis we concentrate on homogenization of the fluctuating response during the non-linear discrete element analysis. The resulting mechanical quantities such as stresses and strains allow a better interpretation of the overall response in terms of continuum mechanics and in particular of the influence of distinct material parameters.

A key question is related to the definition and size of an RVE. On the one hand it should not be too large being still able capturing local effects like evolving shear bands. On the other hand it should be big enough avoiding small scale fluctuations, see Section 5.5.

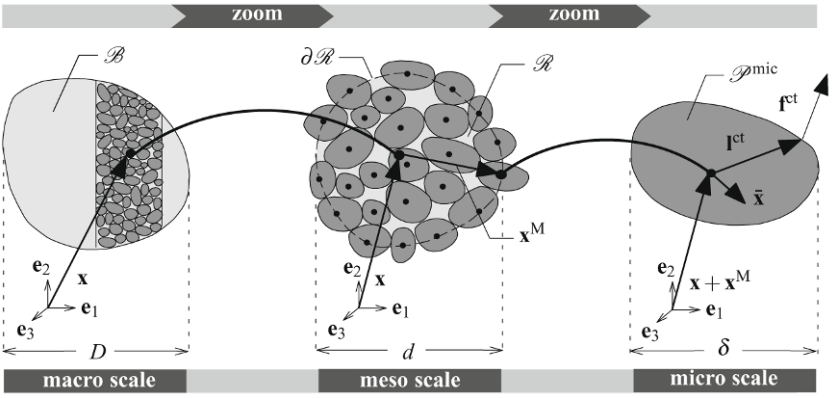


**Fig. 9** Structure consisting of particle ensembles (RVE)

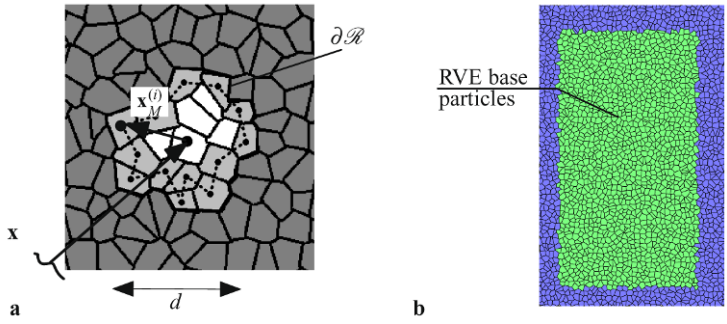


**Fig. 10** Representative Volume Element (RVE): (a) definition and (b) base particles

## 5.2 *Representative Volume Element (RVE)*

A particle ensemble with $N$ particles in diameter, denoted as RVE$N$, is cut out around each so-called base particle in the center of the RVE for which the homogenized variables are determined, see Figure 10a. These are all particles inside the structure leaving out the particles close to its edge (Figure 10b) because the RVEs are not complete and not representative anymore. The size of the RVE defined at the beginning is not changed during the non-linear analysis. The variables are plotted on the base particle for which they are calculated.

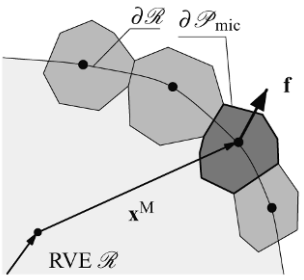


**Fig. 11** Boundary of RVE with force **f**

## *5.3 Averaging Procedure*

### 5.3.1 Stresses

According to the scale separation argument $d/D$ is sufficiently small so that the volumetric contributions to the balance equations may be neglected compared to the surface contributions. It means that only the forces **f** of the boundary particles will enter the averaged balance equation, see Figure 11. Based on this assumption the balance of momentum reads

$$\operatorname{div}\mathbf{T} = \mathbf{0}\,; \qquad \mathbf{0} = \int_{\mathscr{R}} \operatorname{div}\mathbf{T}\,\mathrm{d}v = \int_{\partial\mathscr{R}} \mathbf{t}\,\mathrm{d}a = \sum_{i=1}^{n_{\partial\mathscr{R}}} \mathbf{f}_i\,. \tag{17}$$

$\mathbf{T}$ is the Cauchy stress tensor within the RVE volume $\mathscr{R}$; $\mathbf{t}$ is the traction vector on the RVE boundary $\partial\mathscr{R}$. The integral is discretized and replaced by the sum of forces $\mathbf{f}$ at the RVE boundary acting from outside the RVE on the individual particles. $n_{\partial\mathscr{R}}$ is the number of particles on the entire boundary.

The volume average of the stresses $\langle\mathbf{T}\rangle$ taken over the RVE yields

$$\langle\mathbf{T}\rangle = \frac{1}{V}\int_{\mathscr{R}} \mathbf{T}\,\mathrm{d}v \tag{18}$$

where

$$\mathbf{T}^{\text{T}} = \operatorname{div}(\mathbf{x}^{\text{M}} \otimes \mathbf{T}) - \underbrace{\mathbf{x}^{\text{M}} \otimes \operatorname{div}\mathbf{T}}_{=\mathbf{0}}\,. \tag{19}$$

$\mathbf{x}^{\text{M}}$ is the position vector from the RVE center to the boundary particle center. Following Eq. (17) the last term in Eq. (19) vanishes. Inserting (19) into (18) leads to

$$\langle\mathbf{T}^{\text{T}}\rangle = \frac{1}{V}\int_{\partial\mathscr{R}} (\mathbf{x}^{\text{M}}\otimes\mathbf{T})\mathbf{n}\,\mathrm{d}a - \underbrace{\frac{1}{V}\int_{\mathscr{R}} \mathbf{x}^{\text{M}} \otimes \operatorname{div}\mathbf{T}\,\mathrm{d}v}_{=\mathbf{0}} = \frac{1}{V}\int_{\partial\mathscr{R}} \mathbf{x}^{\text{M}}\otimes\underbrace{\mathbf{T}\mathbf{n}}_{\mathbf{t}}\,\mathrm{d}a = \langle\mathbf{T}\rangle^{\text{T}}\,. \tag{20}$$

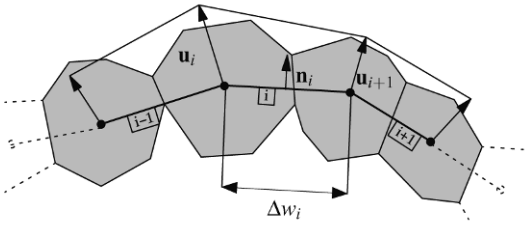


**Fig. 12** Displacement field at RVE boundary

Using Eq. (17) this yields

$$\langle \mathbf{T} \rangle = \frac{1}{V} \int_{\partial \mathcal{R}} \mathbf{t} \otimes \mathbf{x}^{\mathrm{M}} \, \mathrm{d}a = \frac{1}{V} \sum_{i=1}^{n_{\partial \mathcal{R}}} \mathbf{f}_i \otimes \mathbf{x}_i^{\mathbf{M}} \, . \tag{21}$$

Again the integral has been replaced by the sum over all boundary particles in the sense of the discrete element concept.

### 5.3.2 Strains

The same concept of homogenization can be applied to kinematic variables. For the average strain we start from the discrete displacements of boundary particles from which a continuous polygonal displacement field can be developed, see Figure 12. This linear displacement field is integrated along the RVE boundary and inserted into the averaged strain expression

$$\begin{aligned} \langle \boldsymbol{\varepsilon}_{\mathrm{sym}} \rangle &= \frac{1}{V} \int_{\mathcal{R}} \boldsymbol{\varepsilon}_{\mathrm{sym}} \, \mathrm{d}V \\ &= \frac{1}{V} \int_{\partial \mathcal{R}} \frac{1}{2} (\mathbf{u} \otimes \mathbf{n} + \mathbf{n} \otimes \mathbf{u}) \, \mathrm{d}A \\ &= \frac{1}{V} \sum_{i=1}^{n_{\partial \mathcal{R}}} \frac{1}{4} \Delta w_i [(\mathbf{u}_i + \mathbf{u}_{i+1}) \otimes \mathbf{n}_i + \mathbf{n}_i \otimes (\mathbf{u}_i + \mathbf{u}_{i+1})] \, . \end{aligned} \tag{22}$$

The procedure ends in a summation along all boundary particles leading to the strain field projected on the base particle.

In a similar way other variables can be obtained, for example the spatial velocity gradient. It is also mentioned that this consistent homogenization satisfies the balance of energy, known as the Hill condition.

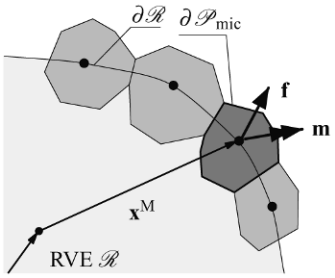


**Fig. 13** Boundary of RVE with force **f** and moment **m**

## *5.4 Extension to Higher Order Continua*

In order to capture the microstructure of a material in the neighborhood of a material point higher order continua have been introduced in the past. If these neighborhood influences are taken into account the homogenization of the response for the particle ensemble can be extended to these theories allowing deriving higher order dynamic and kinematic variables. Here we concentrate on a micropolar (Cosserat) continuum and briefly mention the possibilities for a gradient continuum.

### 5.4.1 Micropolar Continuum

The key assumption in this case is that the forces on the outer surfaces of the boundary particles are transferred to the center of the elements producing extra moments in addition to the forces already seen above, see Figure 13 compared to Figure 11. The extra moments **m** are due to the contact forces $\mathbf{f}^{\text{ct}}$ as well as the contributions $\mathbf{m}^{\text{ch}}$ from beams or interfaces representing cohesion with the $\tilde{n}_{\text{ct}}$ and $\tilde{n}_{\text{ch}}$ particles outside the RVE, respectively

$$\mathbf{m} = \mathbf{m}^{\text{ct}} + \mathbf{m}^{\text{ch}} = \sum_{j=1}^{\tilde{n}_{\text{ct}}} \mathbf{l}_j^{\text{ct}} \times \mathbf{f}_j^{\text{ct}} + \sum_{j=1}^{\tilde{n}_{\text{ch}}} \mathbf{m}_j^{\text{ch}} \,. \tag{23}$$

$\mathbf{l}^{\text{ct}}$ is the so-called branch vector, see Figure 1.

In the averaging process two moments can be identified, namely the continuum moment or moment of the stress distribution **M** and the couple stress tensor $\bar{\mathbf{M}}$ of the Cosserat theory

$$\begin{aligned} \langle \mathbf{M} + \bar{\mathbf{M}} \rangle &= \frac{1}{V} \int_{\partial\mathscr{R}} \left( \mathbf{M} + \bar{\mathbf{M}} \right) \mathbf{n} \otimes \mathbf{x}^{\text{M}} \, \mathrm{d}a \\ &= \frac{1}{V} \sum_{i=1}^{n_{\partial\mathscr{R}}} (\mathbf{x}_i^{\text{M}} \times \mathbf{f}_i + \mathbf{m}_i) \otimes \mathbf{x}_i^{\text{M}} \end{aligned} \tag{24}$$

with

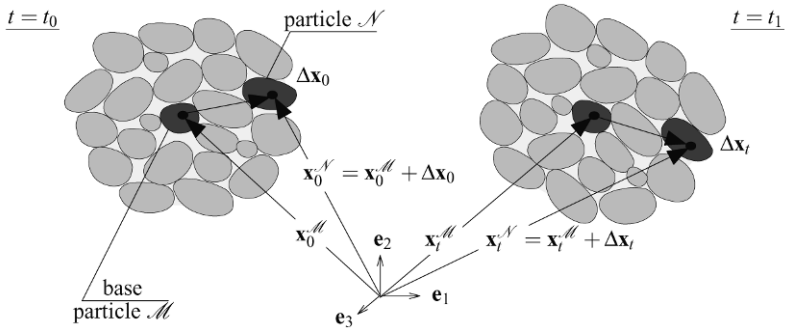


**Fig. 14** Particle ensemble in reference and actual configuration

$$\langle \bar{\mathbf{M}} \rangle = \frac{1}{V} \sum_{i=1}^{n_{\partial\mathcal{R}}} \mathbf{m}_i \otimes \mathbf{x}_i^{\mathrm{M}} . \tag{25}$$

It is worth mentioning that moments on a mesoscale are necessary transferring the particle concept through the homogenization procedure into an enhanced continuum theory, in the present case a macroscopic Cosserat method. If the moments are not taken into account, the couple stresses vanish and the stress tensor becomes symmetric.

In a similar process average values for kinematic variables like rotations and curvatures or additional quantities like energies can be derived. Further details for the homogenization process are given in [7, 12].

### 5.4.2 Gradient Continuum

In this case the key idea is an enhanced kinematic description of an RVE via a Taylor series approximation for the difference vector of two particles, see Figure 14. In other words higher gradients of deformations are taken into account in the homogenization procedure. In this way the intrinsic statistical feature of the heterogeneous material is automatically included. For the homogenization of the kinematics the position vector of a target particle $\mathcal{N}$ is expanded in a vector Taylor series around the base particle $\mathcal{M}$

$$\begin{aligned} \mathbf{x}_t^{\mathcal{N}} &= \frac{1}{0!}\mathbf{x}_t^{\mathcal{M}} + \frac{1}{1!}\frac{\partial \mathbf{x}_t^{\mathcal{M}}}{\partial(\mathbf{x}_0^{\mathcal{M}})} \cdot \Delta\mathbf{x}_0 + \frac{1}{2!}\frac{\partial^2 \mathbf{x}_t^{\mathcal{M}}}{\partial(\mathbf{x}_0^{\mathcal{M}})^2} : \Delta\mathbf{x}_0 \otimes \Delta\mathbf{x}_0 \\ &\quad + \frac{1}{3!}\frac{\partial^3 \mathbf{x}_t^{\mathcal{M}}}{\partial(\mathbf{x}_0^{\mathcal{M}})^3} \vdots \Delta\mathbf{x}_0 \otimes \Delta\mathbf{x}_0 \otimes \Delta\mathbf{x}_0 + \tilde{\mathbf{w}} \\ &= \mathbf{x}_t^{\mathcal{M}} + \underbrace{\mathbf{F} \cdot \Delta\mathbf{x}_0 + \mathbf{G} : \Delta\mathbf{x}_0 \otimes \Delta\mathbf{x}_0 + \mathbf{K} \vdots \Delta\mathbf{x}_0 \otimes \Delta\mathbf{x}_0 \otimes \Delta\mathbf{x}_0}_{\Delta\mathbf{x}_t^{\text{approx}}} + \tilde{\mathbf{w}} . \end{aligned} \tag{26}$$

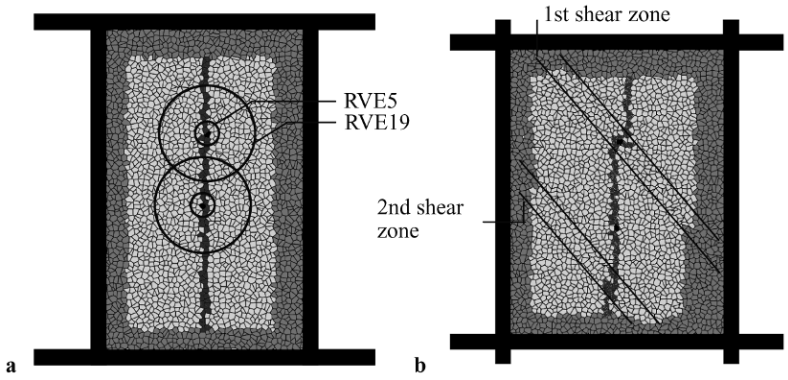


**Fig. 15** Biaxial test: (a) initial and (b) deformed structure

In the present equation the series is truncated after terms of third order leaving the higher order terms in the residual vector $\tilde{\mathbf{w}}$. Equation (26) intrinsically contains the deformation gradient $\mathbf{F}$ and the second and third deformation gradient tensors $\mathbf{G}$ and $\mathbf{K}$. All deformation tensors are evaluated in the sense of an RVE and represent average quantities.

For the sake of brevity, the reader is referred to [7] where further details of the homogenization procedure are given.

## *5.5 Size of RVE*

With the following example we want to discuss the above mentioned dilemma between a too big and a too small RVE size. It is a biaxial test with about 2500 polygonal particles under constant side pressure $q = 1\,\mathrm{kN/cm^2}$ and a constant increase of velocity of the top and bottom plate (Figure 15). The size of the sample is 64 cm $\times$ 40 cm. The contact models (5) and (8) were used with the material data: Young's modulus $E_{\mathrm{n}}^{(1)} = 100\,\mathrm{kN/cm^2}$, density $\varrho = 5\,\mathrm{g/cm^3}$, $\gamma_{\mathrm{n}} = 10^5$, $\mu_{\mathrm{t}} = 0$, $\gamma_{\mathrm{t}} = 0$; the time increment is $\Delta t = 1 \cdot 10^{-6}$ s. No cohesion is assumed. In the initial and the deformed structure the vertical center line is marked easing the identification of the particles after deformation. In the right picture two evolving shear zones are indicated clearly visualized by the two offsets of the marked particles.

Figure 16 shows the overall response in form of a normalized load-displacement relation. After a certain load is reached shear bands evolve resulting in a sudden brittle failure. This part is zoomed out in the figure indicating three stages, marked by ① to ③. In Figure 17 the vertical stress normalized to the average stress ("load") obtained by averaging via RVEs is shown. The vertical stresses are evaluated by homogenization along the marked vertical center line from the bottom to the top.

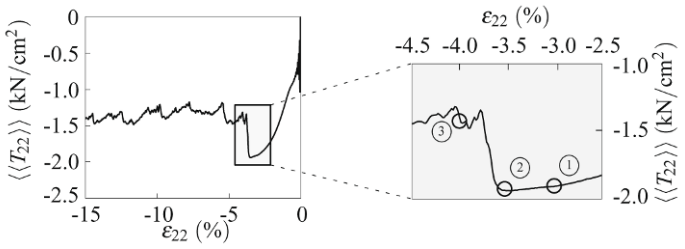


**Fig. 16** Biaxial compression test: normalized load-displacement diagram

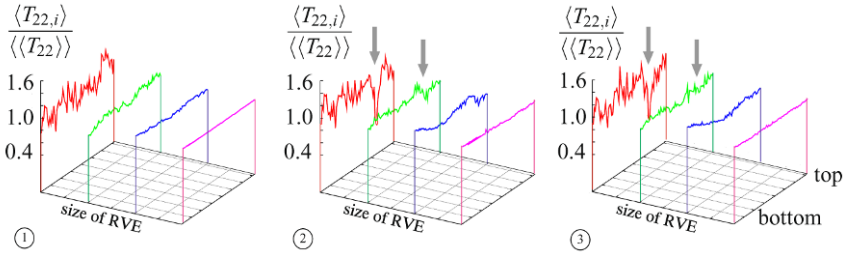


**Fig. 17** Influence of size of RVE: three stages ① to ③ for RVE3, RVE7, RVE13 and RVE39 (at each stage from left to right)

Four different sizes of RVE ranging from a very small RVE3 to an extremely large one RVE39 are investigated for the three loading stages ① to ③. It can be clearly recognized that the small RVE shows distinct fluctuations even anticipating shear banding with diminishing stresses in stage ②. The bigger the RVE the more the stresses are smoothed out along the line, so no local effects can be seen anymore. Evaluating other samples it turned out that the size RVE5 represents a sufficient compromise between too small (undesired fluctuations) and too large (too much smoothing) RVEs.

# 6 Examples

## *6.1 Samples without Cohesion*

### 6.1.1 Biaxial Compression Test of Granular Material

In contrast to the example discussed in Section 5.5 with a dense material, a porous granular material is investigated first followed by a wide biaxial compression test. The mesh generation follows the principles producing a random lattice via Voronoi tessellation from which a dense particle sample without pores is derived [19], see Figure 18 (stage ①). In the next step all particles are randomly scaled down by

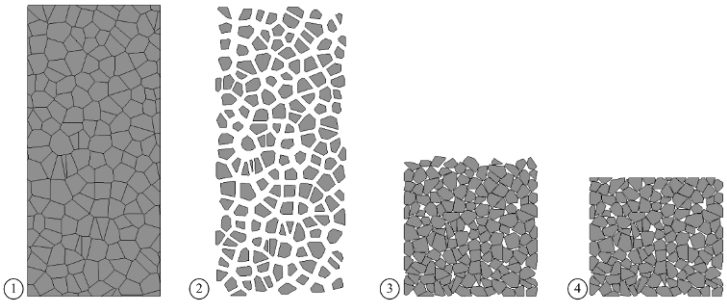


**Fig. 18** Construction of porous packing with random scaling by 30–60%

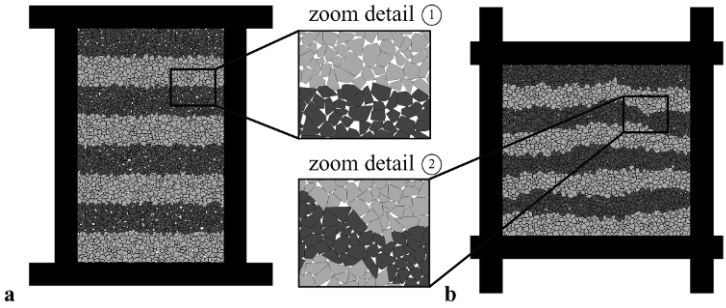


**Fig. 19** (a) Initial and (b) deformed state of porous biaxial test

a given value (stage ②); they also may be rotated by a statistically measure. All particles are positioned into a box applying gravity load through the DEM methodology. When all particles come to rest (stage ③) the top of the sample is cut getting a smooth boundary (stage ④).

The concept is applied to the porous sample shown in Figure 19 with the same data as the previous example in Section 5.5. In the deformed state no clear shear band could be observed, however a zoom indicates a distinct thickness change of the zone marked in dark grey. A comparison of both zoomed details reveals the clear densification of the sample.

Next the height to width ratio of dense specimen, investigated in Section 5.5, is changed from 1 : 1.6 to 1 : 0.37 without modifying the test set-up. Now the rectangular block with 38 cm × 102 cm consists of 3800 particles. After vertical loading distinct zig-zag shear bands evolve (Figure 20) which are also clearly indicated by the horizontal strains $\langle \varepsilon_{11} \rangle$ in Figure 21.

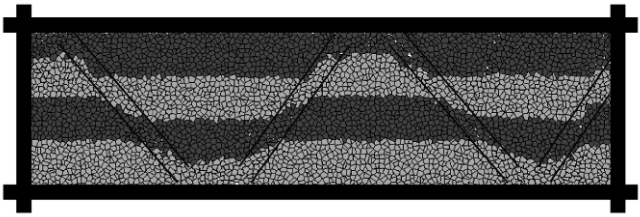

**Fig. 20** Wide biaxial compression test: deformation at late stage of the simulation

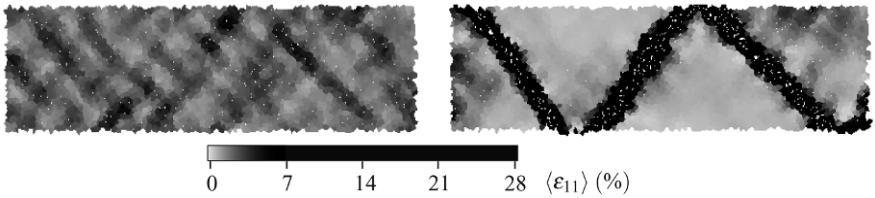


**Fig. 21** Wide biaxial compression test: horizontal strains at early (left) and late (right) stage of the simulation

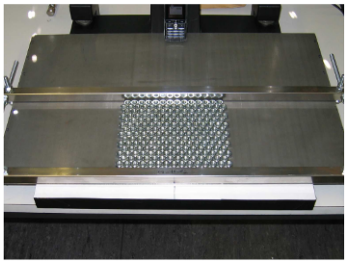

**Fig. 22** Experiment with steel nuts

### 6.1.2 Uniaxial Compression of Model Material

The following conceptual test has been chosen in order to investigate the quality of the present DEM on regular particles without a geometrical bias. A rectangular sample of 217 hexagonal steel nuts (17 cm × 19 cm) lying on a background steel plate has been tested under uniaxial compression, see experimental setup in Figure 22. One loading platen is moved to the front by a constant low velocity $\hat{v}_2 = -6.2 \cdot 10^{-4}$ m/s whereas the other one is fixed. For the simulation the geometry of the nuts with a hole and slightly round corners has been approximated by sharp edged solid hexagons. Contact in normal (7) and tangential (9) direction as well as with the background plate (10) is modeled. The data for the model without cohesion are experimentally verified: $\varrho = 3.3$ g/cm$^3$, $\mu_\mathrm{t} = 0.29$ and $\mu_\mathrm{b} = 0.26$; the stiffnesses are chosen as $E_\mathrm{n}^{(2)} = 1.0 \cdot 10^2$ N/cm$^4$, $E_\mathrm{t} = 2.9 \cdot 10^2$ N/cm$^2$, $E_\mathrm{b} = 8.4 \cdot 10^2$ N/cm$^3$ and the time increment as $\Delta t = 1 \cdot 10^{-5}$ s. In order to break symmetry of the sample the normal contact stiffness of the particle besides the center at the upper row is reduced by 10%.

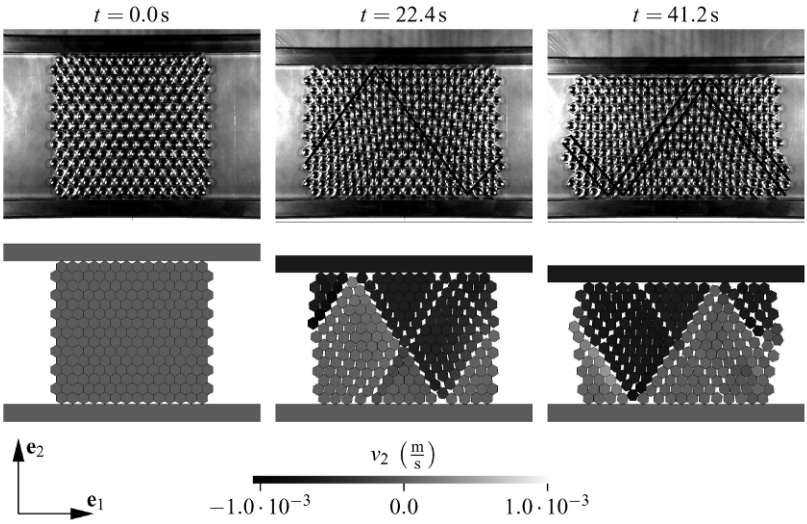


**Fig. 23** Comparison of experiment and simulation

In Figure 23 results from experiment and simulation are compared at different time instants. The grey scale constitutes the velocity in $\mathbf{e}_2$-direction. Both cases initially show a diffuse lateral expansion followed by the evolution of distinct shear bands. The mode shown at $t = 22.4$ s is considerably changed until $t = 41.2$ s. This change is inherent in both, the experiment as well as the DEM simulation.

## *6.2 Samples with Cohesion*

### 6.2.1 L-shape Test

The L-shape specimen is mimicked after a concrete benchmark experimentally tested in [26]. The data of the model material are taken from Section 5.5 using the contact models (5) and (8), however in this case cohesion is modeled by a brittle beam lattice described in Section 4.1; the beams have a Young's modulus of $E = 1000$ kN/cm$^2$; the threshold values for cracking are $\varepsilon_{\max} = 0.03$ and $\phi_{\max} = 3°$. The specimen is loaded by a uniform displacement of the boundary particles at the right edge (Figure 24a). The load-displacement diagram is shown in Figure 24b demonstrating that the failure initiated at the reentrant corner is extremely brittle. Although the data have not been fitted to the tests the crack patterns shown in Figure 25 fit the experimental results qualitatively very well.

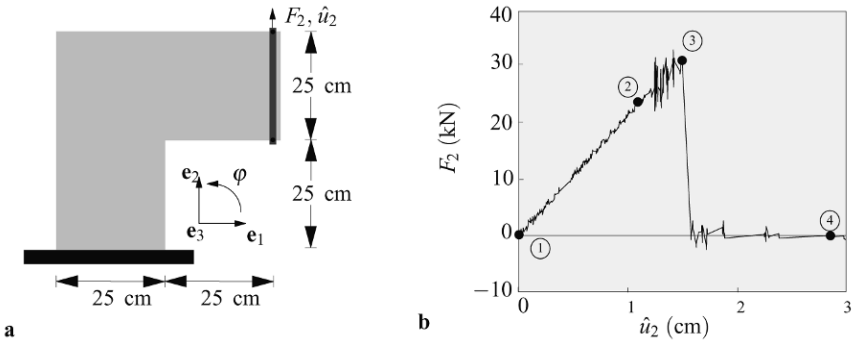


**Fig. 24** (a) L-shape specimen and (b) load-displacement diagram

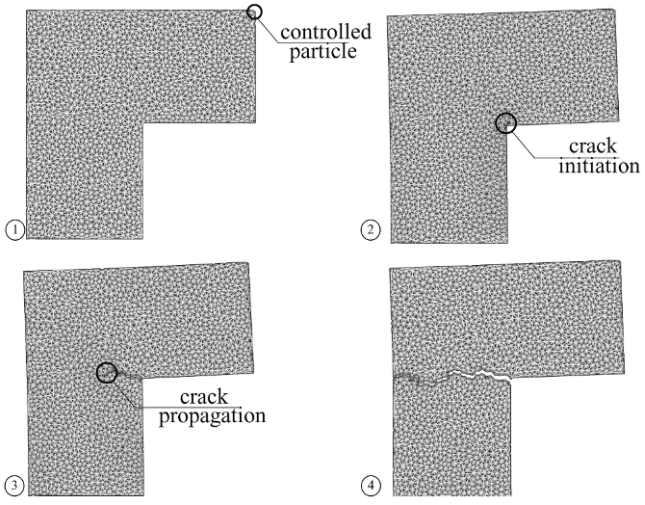


**Fig. 25** L-shape specimen: crack evolution ①–④

### 6.2.2 Uniaxial Compression of Cohesive Model Material

We use the same hexagonal steel nuts as in Section 6.1.2 however bond them together by standard glue. In this case the sample stands between two glass panes in the testing device, see Figure 26a. The friction between particles and panes is so low that it could be neglected. Again a prescribed velocity $\hat{v}_2 = -3.3 \cdot 10^{-5}$ m/s is applied to the upper row of particles leaving the other degrees of freedom free to move. For the present study the cohesion between particles (adhesion through glue) is modeled by the beam with damage, confer to Section 4.2. The data are $\varrho = 3.3$ g/cm$^3$, $E = 28$ N/cm$^2$, $\varepsilon_0 = 1.1 \cdot 10^{-3}$, $\varepsilon_\mathrm{m} = 2.3 \cdot 10^{-1}$; the time increment is chosen as $\Delta t = 1 \cdot 10^{-4}$ s. Figure 26b compares the particle samples with 22 particles for experiment and simulation in the undeformed configuration ① and

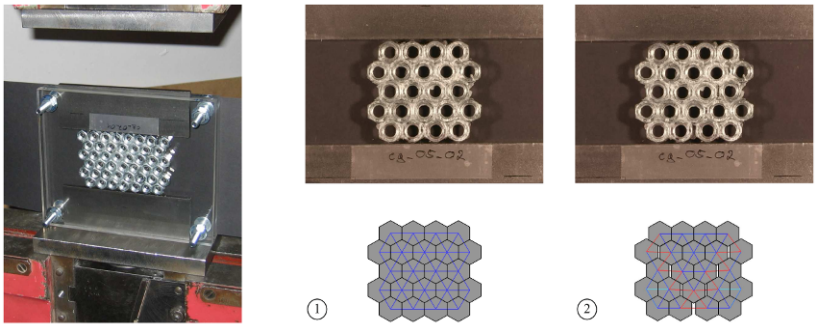


**Fig. 26** (a) Experiment with glued steel nuts and (b) comparison of experiment and simulation at undeformed ① and deformed ② stage

deformed stage ②; the figure also shows the detached glue connections in stage ② where the respected beams of the overlay lattice have already reached the descending softening branch and are damaged. The horizontal beams are mainly elongated whereas the diagonal ones are essentially sheared. The pattern of localization is identical to that of the simulation.

For three experiments the load-displacement diagrams are displayed in Figure 27 and supplemented by the smooth curve from simulation applying the beam with damage. Although geometry and material of the nuts do not differ very much from each other the scatter of the results for all three experiments is clear; the deviation is caused by the rather primitive gluing process. On the other hand the simulation represents a kind of overall mean response having a lower failure load though. The rather smooth transfer into the post-critical regime in the experiments is due to the more ductile failure of the glue under shear compared to the material model applied in the analysis. Increasing the strains $\varepsilon_0$ and $\varepsilon_m$ at beginning and end of softening (see Figure 3a) leads to the expected results, namely an increase of failure load with a steeper descend for $\varepsilon_0$ and increased energy dissipation for higher values of $\varepsilon_m$ without a change of the peak load.

### 6.2.3 Modeling of Microstructure for Concrete under Uniaxial Compression

For a detailed investigation of concrete the microstructure has to be modeled differentiating between stiffness and strength of aggregates, matrix and their bond layer, see Figure 28a. According to van Mier et al. [22] the ratios for stiffnesses and strengths for all three phases are

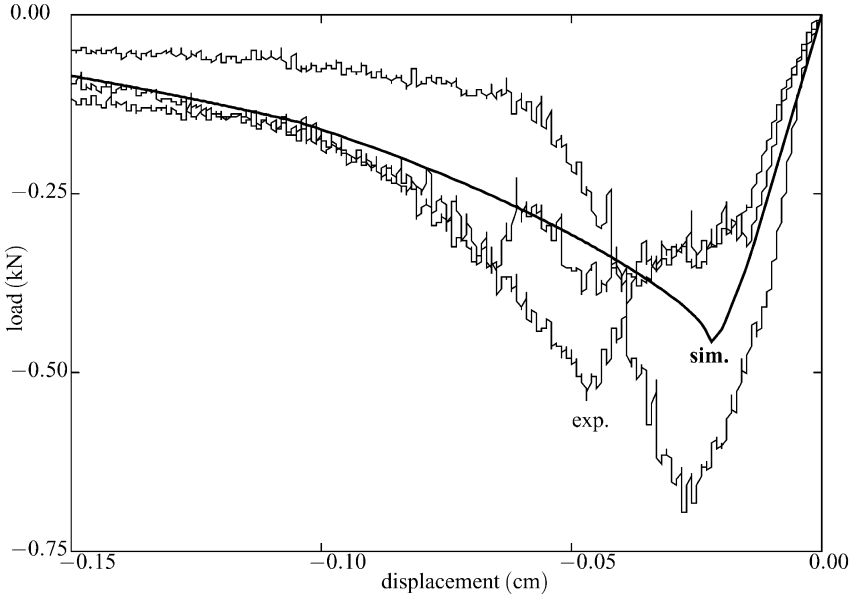


**Fig. 27** Load-displacement diagram: three experiments with glued particles (thin lines) and simulation (thick line)

$$\frac{k_{\mathrm{n}}^{(\mathrm{b})}}{k_{\mathrm{n}}^{(\mathrm{m})}} = 0.1\,; \qquad \frac{k_{\mathrm{t}}^{(\mathrm{b})}}{k_{\mathrm{t}}^{(\mathrm{m})}} = 0.4\,; \qquad \frac{\sigma_{\mathrm{n/t}}^{\max,(\mathrm{b})}}{\sigma_{\mathrm{n/t}}^{\max,(\mathrm{m})}} = 0.25$$
$$\frac{k_{\mathrm{n}}^{(\mathrm{a})}}{k_{\mathrm{n}}^{(\mathrm{m})}} = 2.8\,; \qquad \frac{k_{\mathrm{t}}^{(\mathrm{a})}}{k_{\mathrm{t}}^{(\mathrm{m})}} = 2.8\,; \qquad \frac{\sigma_{\mathrm{n/t}}^{\max,(\mathrm{a})}}{\sigma_{\mathrm{n/t}}^{\max,(\mathrm{m})}} = 100\,.$$

The cohesive connections between grains are stiffer and have higher strength than those between matrix particles. The connections at the bond layers between grain and matrix particles are in turn even less stiff and fail at lower loading. The elasto-plastic interface described in Section 4.3 is adopted modeling the cohesion for all three materials. The lattice shown in Figure 28b is only added for visualization of the respective bond condition during loading.

For the matrix following properties are chosen: normal and tangential stiffnesses $k_{\mathrm{n}}^{(\mathrm{m})} = 2000$ kN/cm$^2$, $k_{\mathrm{t}}^{(\mathrm{m})} = 600$ kN/cm$^2$; fracture energies $G_{\mathrm{f,n}}^{(\mathrm{m})} = 4.996 \cdot 10^{-4}$ kN/cm$^2$, $G_{\mathrm{f,t}}^{(\mathrm{m})} = 5.988 \cdot 10^{-3}$ kN/cm$^2$. The yield stresses are statistically distributed for each interface about $\pm 10\%$ the average values $\sigma_{\mathrm{n}}^{\max,(\mathrm{m})} = 0.04$ kN/cm$^2$, $\sigma_{\mathrm{t}}^{\max,(\mathrm{m})} = 0.12$ kN/cm$^2$. The shape parameters are $\varphi = 26.6°$, $\gamma = 10°$, $\psi = 0°$ and the density is $\varrho = 2.5$ g/cm$^3$. The contact models (5) and (8) have been used with the contact stiffness $E_{\mathrm{n}}^{(1)} = 100$ kN/cm$^2$. Viscous damping as well as friction are set to zero ($\gamma_{\mathrm{n}} = \gamma_{\mathrm{t}} = 0$; $\mu_{\mathrm{t}} = 0$) and the time step is chosen as $\Delta t = 5 \cdot 10^{-7}$ s.

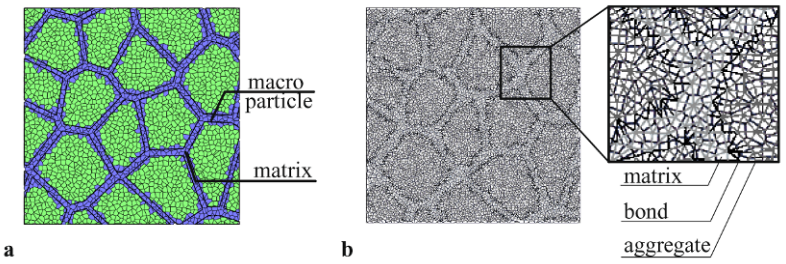


**Fig. 28** Microstructure with matrix, bond and aggregate

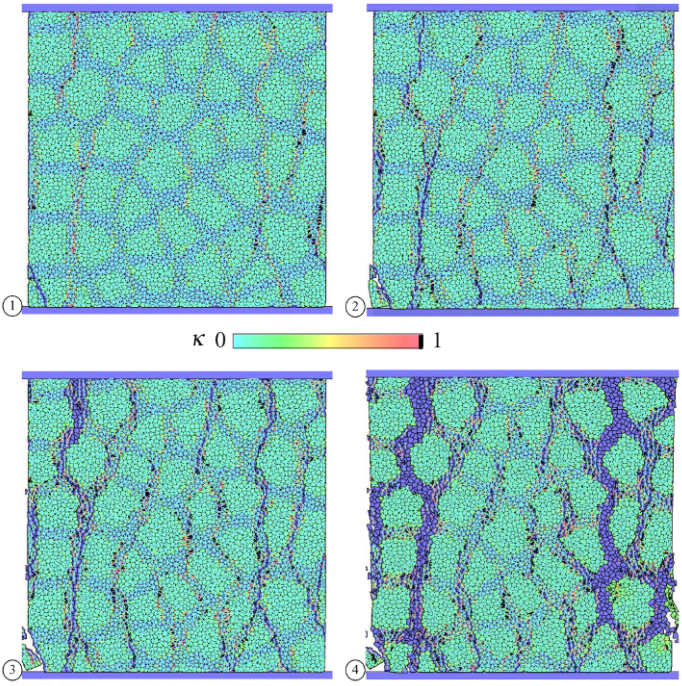


**Fig. 29** Failure evolution during simulation sim$^{*1}$

Applying this microstructure enhanced discrete element model uniaxial displacement driven compression tests are simulated, see the evolution of simulation sim$^{*1}$ in Figure 29.

In Figure 30b the black lines mark the locations where the cohesive interfaces are completely eliminated, i.e. $\kappa = 1$. The cracks run primarily along the aggregate boundaries as it is typical for concrete. In Figure 30a the nominal stresses are plotted versus the nominal strain representing a load-displacement diagram. Besides simulation sim$^{*1}$ the average $\langle \text{sim}^{*i} \rangle$ of seven simulations with different statistically

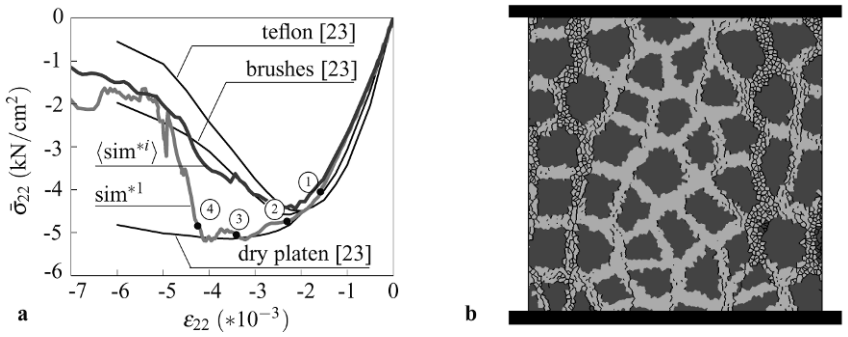


**Fig. 30** (a) Load-displacement diagram and (b) eliminated interfaces of sim$^{*1}$ at stage ④

varied samples are shown and compared to three experimental results performed with different loading platens by Vonk [23]. The ascending branches as well as peak loads are very well reproduced by the simulation; there is some deviation in the post-critical regime though.

## 7 Conclusions

The response of quasi-brittle materials using polygonal particles is characterized by more realism but also larger complexity and effort compared to circular particles. Besides contact search modeling of cohesion is a further parameter increasing the expense of the simulation. We have discussed three models for cohesion with an increasing effort. The lattice model of brittle beams is extremely efficient but results in a sudden failure mechanism. On the other side of the spectrum the interface model is the most realistic version; however it is also the most time consuming model. The beam with damage is a compromise between the two other models. Its quality has been checked also in relation to experimental results obtained from conceptual tests using conventional steel nuts as particles; by this the geometrical bias usually inherent in a sample of particles is diminishing. The tests have been performed for ensembles of particles which are loosely connected or glued together representing cohesion (adhesion). It turned out that the agreement between experiments and simulations are qualitatively excellent and quantitatively sufficient considering the substantial scatter of the material parameters.

## Acknowledgement

The authors are indebted for the financial support of the German Research Foundation (DFG) within the research project "Fragmentierung kohäsiver Reibungsmaterialien mit diskretem Partikelmodell" under grant no. RA 218/22-1.

## References

1. Allen, M.P., Tildesley, D.J., *Computer Simulation of Liquids*. Oxford University Press, Oxford, 1987.
2. Bićanić, N., Discrete element methods. In: *Encyclopedia of Computational Mechanics: Volume 1: Fundamentals*, Stein, E., de Borst, R., Hughes, T.J.R. (eds.), pp. 311–337. Wiley, Chichester, 2004.
3. Bićanić, N., Discrete element methods. In: *The Finite Element Method for Solid and Structural Mechanics*, 6th edn., Zienkiewicz, O.C., Taylor, R.L., pp. 245–277. Elsevier, Oxford, 2005.
4. Cundall, P.A., A discontinuous future for numerical modelling in geomechanics. *Geotech. Eng.* 149:41–47, 2001.
5. Cundall, P.A., Hart, R.D., Numerical modelling of discontinua. *Eng. Comput.* 9:101–113, 1992.
6. Cundall, P.A., Strack, O.D.L., A discrete numerical model for granular assemblies. *Géotechnique* 29:47–65, 1979.
7. D'Addetta, G.A., Discrete models for cohesive frictional materials. Ph.D. Thesis, Bericht Nr. 42, Institut für Baustatik, Universität Stuttgart, Germany, http://elib.uni-stuttgart.de/opus/volltexte/2004/1943/pdf/diss_gad.pdf, 2004.
8. D'Addetta, G.A., Ramm, E., A microstructure-based simulation environment on the basis of an interface enhanced particle model. *Granul. Matter* 8:159–174, 2006.
9. D'Addetta, G.A., Kun, F., Herrmann, H.J., Ramm, E., From solids to granulates – Discrete element simulations of fracture and fragmentation processes in geomaterials. In: *Continuous and Discontinuous Modelling of Cohesive Frictional Materials*, Vermeer, P.A., Diebels, S., Ehlers, W., Herrmann, H.J., Luding, S., Ramm, E. (eds.), Lecture Notes in Physics, vol. 586, pp. 231–258. Springer, Berlin, 2001.
10. D'Addetta, G.A., Kun, F., Ramm, E., On the application of a discrete model to the fracture process of cohesive granular materials. *Granul. Matter* 4:77–90, 2002.
11. D'Addetta, G.A., Schneider, B., Ramm, E., Particle models for cohesive frictional materials. In: *Computational Modelling of Concrete Structures, Proceedings of EURO-C 2006*, Meschke, G., de Borst, R., Mang, H., Bićanić, N. (eds.), Mayrhofen, Austria, 27–30 March 2006, pp. 269–280. Taylor & Francis, London, 2006.
12. Ehlers, W., Ramm, E., Diebels, S., D'Addetta, G.A., From particle ensembles to Cosserat continua: Homogenization of contact forces towards stresses and couple stresses. *Int. J. Solids & Struct.* 40:6681–6702, 2003.
13. Feng, Y.T., Owen, D.R.J., A 2D polygon/polygon contact model: Algorithmic aspects. *Eng. Comput.* 21:265–277, 2004.
14. Gear, C.W., *Numerical Initial Value Problems in Ordinary Differential Equations*. Prentice-Hall, Englewood Cliffs, 1971.
15. Hashin, Z., Analysis of composite materials – A survey. *ASME J. Appl. Mech.* 50:481–505, 1983.
16. Herrmann, H.J., Hansen, A., Roux, S., Fracture of disordered, elastic lattices in two dimensions. *Phys. Rev. B* 39:637–648, 1989.
17. Kun, F., Herrmann, H.J., A study of fragmentation processes using a discrete element method. *Comput. Methods Appl. Mech. Eng.* 138:3–18, 1996.

18. Kun, F., D'Addetta, G.A., Herrmann, H.J., Ramm, E., Two-dimensional dynamic simulation of fracture and fragmentation of solids. *Comput. Assist. Mech. Eng. Sci.* 6:385–402, 1999.
19. Moukarzel, C., Herrmann, H.J., A vectorizable random lattice. *J. Stat. Phys.* 68:911–923, 1992.
20. Pöschel, T., Schwager, T., *Computational Granular Dynamics: Models and Algorithms*. Springer, Berlin, 2005.
21. Tillemans, H.-J., Herrmann, H.J., Simulating granular solids under shear. *Phys. A* 217:261–288, 1995.
22. van Mier, J.G.M., Schlangen, E., Vervuurt, A., van Vliet, M.R.A., Damage analysis of brittle disordered materials: Concrete and rock. In: *Mechanical Behaviour of Materials, Proceedings of the ICM7*, Bakker, A. (ed.), pp. 101–126. Delft University Press, Delft, 1995.
23. Vonk, R., Influence of boundary conditions on softening of concrete loaded in compression. Report TUE/BKO 89.14, Faculteit Bouwkunde, Technische Universiteit Eindhoven, The Netherlands, 1989.
24. Vonk, R., Softening of concrete loaded in compression. Ph.D. Thesis, Technische Universiteit Eindhoven, The Netherlands, 1992.
25. Williams, J.R., O'Connor, R., Discrete element simulation and the contact problem. *Arch. Comput. Methods Eng.* 6:279–304, 1999.
26. Winkler, B.J., Traglastuntersuchungen von unbewehrten und bewehrten Betonstrukturen auf der Grundlage eines objektiven Werkstoffgesetzes für Beton. Ph.D. Thesis, Institut für Baustatik, Festigkeitslehre und Tragwerkslehre, Leopold-Franzens-Universität Innsbruck, Austria, 2001.